PAPER • OPEN ACCESS

Validation of a synthetic fast ion loss detector model for Wendelstein 7-X

View the article online for updates and enhancements.

Validation of a synthetic fast ion loss detector model for Wendelstein 7-X

A. LeViness[1,*]⬤, S.A. Lazerson[2]⬤, A. Jansen van Vuuren[3]⬤, J. Rueda-Rueda[4]⬤,
M. Beurskens[5]⬤, S. Bozhenkov[5]⬤, K.J. Brunner[5]⬤, O.P. Ford[5]⬤, G. Fuchert[5]⬤,
M. Garcìa-Muñoz[4]⬤, M. Isobe[6]⬤, C. Killer[5]⬤, J. Knauer[5]⬤, K. Ogawa[6]⬤, N. Pablant[1]⬤,
E. Pasch[5], P. Poloskei[5]⬤, T. Romba[5]⬤ and the W7-X Team[a]

[1] Princeton Plasma Physics Laboratory, Princeton, NJ, United States of America
[2] Gauss Fusion GmbH, Garching, Germany
[3] Swiss Federal Institute of Technology Lausanne, Lausanne, Switzerland
[4] University of Seville, Seville, Spain
[5] Max Planck Institute for Plasma Physics, Greifswald, Germany
[6] National Institute for Fusion Science, Toki, Japan

E-mail: leviness@pppl.gov

CrossMark

Abstract

We present the first validated synthetic diagnostic for fast ion loss detectors (FILDs) in the Wendelstein 7-X (W7-X) stellarator. This model has been developed on, and validated against experimental data from, a FILD provided by the National Institute for Fusion Science (NIFS-FILD), with potential future applicability to the existing Faraday Cup FILD (FC-FILD) on W7-X as well as the scintillating FILD (S-FILD) currently under development. A workflow combining Monte Carlo codes BEAMS3D and ASCOT5 is used to track fast ions produced by neutral beam injection from the moment of ionization until they are thermalized or lost from the last closed flux surface, and from there to a virtual plane which serves as a projection of the entrance aperture to the FILD. Simulations in ASCOT5 are analyzed via a geometric method to determine the probability of transmission through the FILD aperture and onto the detector as a function of normalized momentum, pitch angle, gyrophase, and position at the virtual plane. This probability is then applied to the simulated ions arriving from the plasma, producing a simulated signal from a computationally tractable number of simulated fast ions. Simulated signals are presented for two W7-X experiments with neutral beam injection and quantitatively compared with experimental measurements from the NIFS-FILD diagnostic. An estimate of the frequency of charge-exchange with neutral particles in the edge is performed, and it is found that this process may have a significant impact on the measured signals.

Keywords: fusion, stellarator, Wendelstein 7-X, diagnostics, fast ions

(Some figures may appear in colour only in the online journal)

---

[a] See Grulke *et al* 2024 (https://doi.org/10.1088/1741-4326/ad2f4d) for the W7-X Team.
[*] Author to whom any correspondence should be addressed.

1. Introduction

1.1. Motivation

The confinement of fast ions is important for any magnetic confinement fusion reactor, as ignition cannot be achieved unless the ions produced in the fusion reaction can be confined for a sufficient amount of time to transfer their energy to the bulk plasma via collisions. For non-reactor plasma experiments as well, confining fast ions is necessary to make efficient use of heating systems such as neutral beam injection (NBI) and ion cyclotron resonance heating (ICRH) and to avoid damage to the walls and sensitive plasma-facing components (PFCs).

Fast ion confinement is a crucial topic for stellarators in particular, as the lack of axisymmetry means that trapped particle orbits are not inherently confined as they are in tokamaks. Stellarators must be numerically optimized for good fast ion confinement, and this optimization is one of the main focuses of stellarator design [1, 2]. As the largest optimized stellarator in the world, verification that the optimization of Wendelstein 7-X (W7-X) truly translates into enhanced performance is an important milestone towards the eventual design of a stellarator fusion pilot plant. The successful neoclassical optimization of thermal energy transport in W7-X has already been verified [3], but the question of fast ion confinement is still an open one.

In order to verify the successful optimization of fast ion confinement in W7-X, information about fast ion losses must be gathered through the use of diagnostics, and computer simulations of fast ions in W7-X must be compared to these measurements in order to show that the losses are in line with our predictions. In addition, measurements are necessary to validate the computational tools we use to predict fast ion losses in the first place, so that these tools can be utilized in the design of future stellarators.

This work will present a validated model for predicting signals to the diagnostics used to measure fast ion losses on W7-X, and will shed light on areas in which our current models may be inadequate.

1.2. Sources of fast ions in Wendelstein 7-X

Beginning in 2018, during the OP1.2b experimental campaign, neutral beams were commissioned for operation on W7-X. W7-X has two neutral beam boxes, each one containing four beam sources. Two sources in one beam box were first operated during this campaign [4], with an additional two sources in the second box commissioned and operated during the 2022–2023 experimental campaign, OP2.1 [5]. In H operation, each beam source can inject around 1.8 MW neutralized power for up to 5 s at a time.

The W7-X NBI system can inject neutral hydrogen (H) or deuterium (D) at 55 or 60 keV, respectively, but has thus far been limited to H operation [4, 5]. At these energies, and a magnetic field strength of 2.5 T (the typical strength on the

magnetic axis of W7-X), H and D have effective gyroradii, defined as the ratio of gyroradius to the minor radius of the device, nearly equivalent to that of 3.5 MeV α particles in the 5.5 T HELIAS 5-B reactor design—this ratio is around 0.019 and 0.028 for the NBI protons and deuterons, respectively, and 0.019 for the fusion alphas in HELIAS, assuming $v_\perp = v_{||} = \sqrt{E/m}$, meaning that these NBI ions can be used as proxies for fusion αs [6], at least when considering neoclassical transport. When taking instabilities into account, these particles are not as similar: the ratio of birth velocity to Alfvén speed is not equivalent, being around 0.59 and 0.44 for H and D NBI ions in a hydrogen plasma in W7-X with a density of 1×10^{20} m^{-3}, while for fusion alphas in a DT plasma in HELIAS with a density of 3×10^{20} m^{-3} (the density at which HELIAS is designed to operate [7]), this ratio would be 2.9—around 5 times larger. This means that alpha particles in HELIAS would be able to drive shear Alfvén waves through the Landau resonance, while NBI ions in W7-X cannot.

The first two NBI sources operated were those labeled 7 and 8, located within beam box NI21 within the upper half of module 2 of the 5-period W7-X, and the additional sources added were sources 3 and 4, located within beam box NI20 within the lower half of module 2. Sources 3 and 7 inject at a more radial angle to the magnetic axis, while sources 4 and 8 inject more tangentially.

1.3. Fast ion loss detectors in Wendelstein 7-X

Fast ion loss detectors (FILDs) are a type of diagnostic used to directly measure escaping fast ions from magnetic confinement devices, and are commonly used in many magnetic fusion experiments, both tokamaks and stellarators [8–28]. The most popular types are the Faraday Cup type, which measures the flux of lost fast ions to a thin metal film as a current, and the scintillating type, which measures the light emitted from a phosphorescent screen when impacted by a fast ion. Both types often make use of a pinhole and collimating structure to distribute fast ion strikes spatially based on their energy and pitch, allowing for resolution of losses in these quantities.

Two FILDs have thus far been implemented on W7-X, both Faraday Cup types: the NIFS-FILD [29], provided by the National Institute for Fusion Science (Toki, Japan), as well as the FC-FILD [30, 31], developed by the Max Planck Institute for Plasma Physics (Greifswald, Germany) and Princeton Plasma Physics Laboratory (Princeton, NJ, USA). The NIFS-FILD was mounted on the multipurpose manipulator (MPM) [32] for several days of experiments in both OP1.2b and OP2.1, while the FC-FILD was permanently implemented on the machine beginning in OP2.1.

In addition, a third scintillating-type FILD, the S-FILD, is currently in development by Princeton Plasma Physics Laboratory, the University of Seville, and the Max Planck Institute for Plasma Physics [33–35]. A complete design has been produced, and the S-FILD is expected to be constructed and implemented on W7-X for an upcoming experimental campaign.
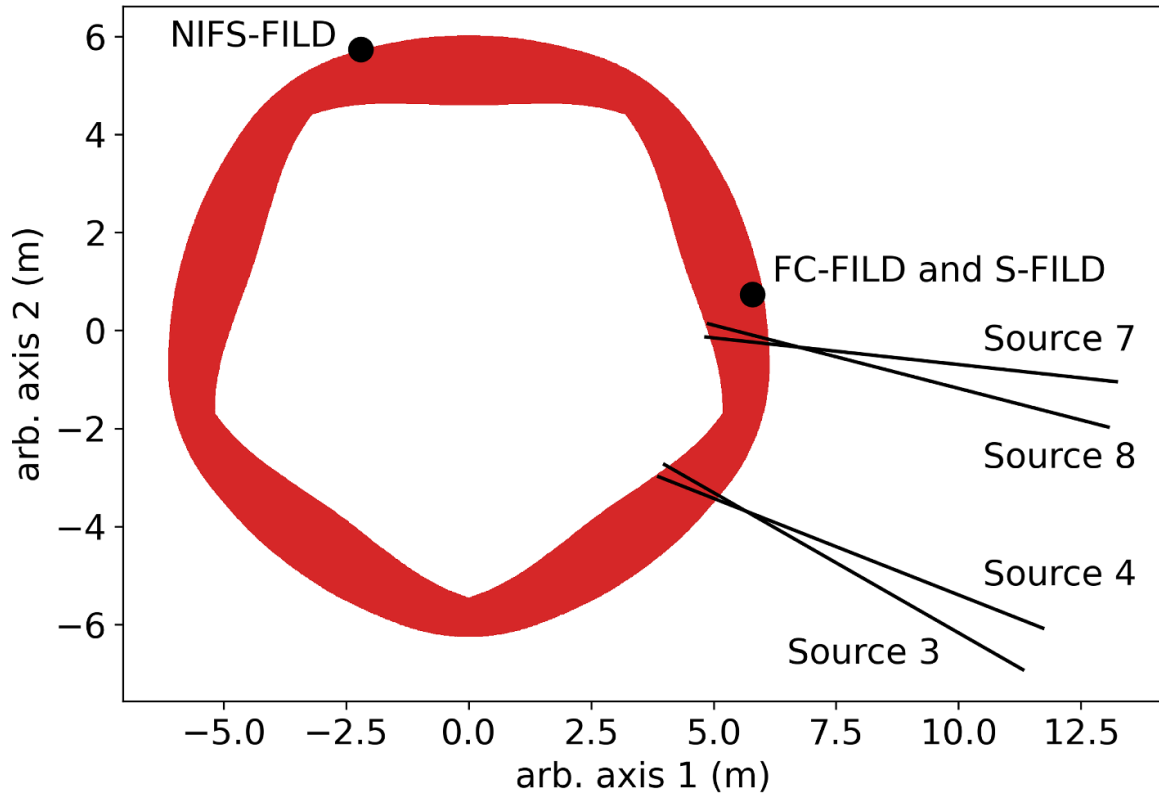
Figure 1. The last closed flux surface of W7-X from the top down, plotted in red, with the four commissioned neutral beam sources and the three existing or planned FILDs.

In figure 1, the position of these three FILDs when fully inserted in relation to the plasma is shown, along with the injection angles of the four commissioned neutral beam sources.

The method in this work was developed for the NIFS-FILD, and initial simulations are presented and compared to experimental data for two W7-X plasmas, one for each experimental campaign with NBI. In the following section, the details of the NIFS-FILD are described.

1.4. NIFS-FILD

The NIFS-FILD is a Faraday Cup FILD consisting of eight metal detectors within a stainless steel, carbon-shielded probe head, which has a pinhole and collimating structure in order to provide energy and pitch resolution of the measured fast ions [29]. In figure 2 is a 3D view of the position of the sensor array and pinhole within the probe head.

Overlaid onto the sensor array in figure 3 is a strike-map showing the average strike location of the fast ions which reach the sensor as a function of a gyroradius-like quantity ($\frac{mv}{|q|B}$, equal to $\frac{v}{v_\perp} r_{\text{gyro}}$—where r_{gyro} is the actual gyroradius—given in units of cm) and pitch angle ($\cos^{-1}\left(\frac{v_{||}}{v}\right)$, given in units of degrees). The exact strike position of any ion depends not only on these quantities but also on the starting gyrophase and the
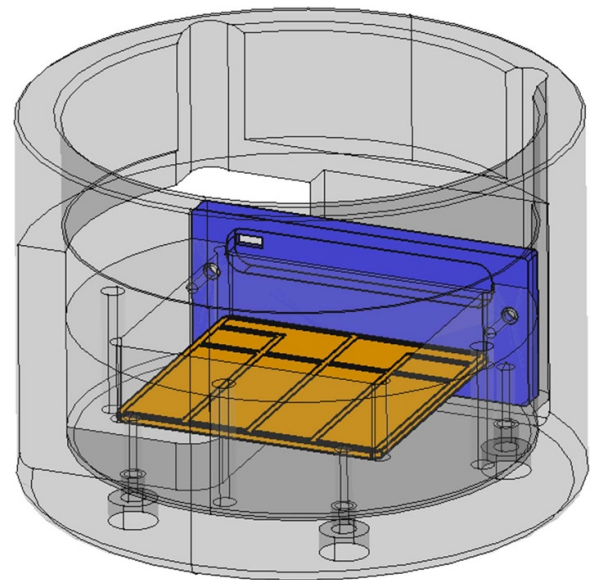
Figure 2. The layout of the NIFS-FILD probe head, including the sensor array (brown), the pinhole and collimating slit (blue), and the stainless steel cap (gray).

ion's initial position within the pinhole; the strike map displayed in this figure is found by taking the average position of all strike locations on the sensor for a given velocity and pitch. The magnetic field used for the simulations in this figure is
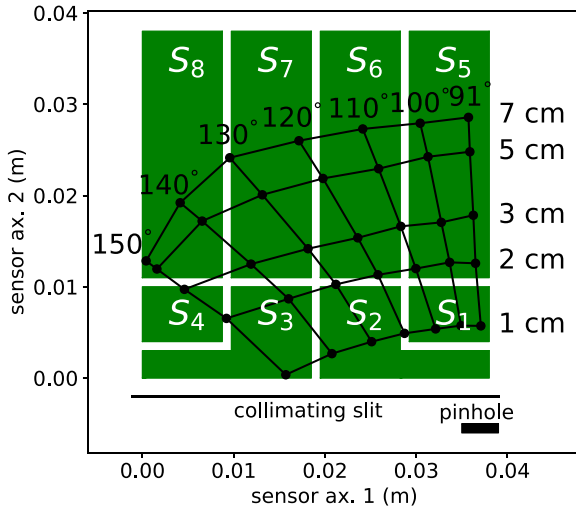
Figure 3. A strike map in pitch angle ($\cos^{-1}\left(\frac{v_{||}}{v}\right)$) and a gyroradius-like quantity ($\frac{mv}{|q|B}$) of the average strike position of fast ions reaching the eight sensors of the NIFS-FILD. This shows which energies and pitch angles we expect to be measured by each sensor.

the W7-X standard configuration with the NIFS-FILD inserted 197 mm.

2. Methods

2.1. Energetic particle simulation codes

Monte Carlo simulations of NBI-created fast ions are performed via a workflow combining the codes BEAMS3D and ASCOT5, very similar to the workflow described in [36]. The density and temperature profiles are taken from experimental measurements with Thomson scattering [37] (for electron density n_e and temperature T_e) and charge exchange recombination spectroscopy, CXRS [38] (for ion temperature T_i). The experimental data points are fit to form profiles and combined with the coil filament geometry as inputs to the free-boundary version of the equilibrium-solving code VMEC [39]. The same inputs are used to calculate the neoclassical radial electric field E_r, toroidal current, and total toroidal flux enclosed by the plasma using the code NEOTRANSP [40], which in turn uses the DKES (Drift Kinetic equation Solver) code, and the resulting self-consistent equilibrium is used as a basis for the simulations.

First, BEAMS3D[7] is used to model neutral beam injection by tracking neutral 'markers' (simulation units representing neutral or charged particles) as they pass through a detailed port geometry and into the plasma, during which time they either collide with the port, are ionized within the plasma, or pass through the plasma to strike the vessel wall ('shine-through'). For these simulations, all beams are taken to inject hydrogen atoms with energies of 55, 27.5, and 18.3 keV (from acceleration within the neutral beam source boxes of H^+, H_2^+,

and H_3^+) with estimated power fractions of 51%, 30%, and 19%, respectively [41]. The number of markers can be set by the user, and each marker is given a weight which corresponds to the total number of real particles represented by each marker. The ionization of the beam is calculated following the validated deposition model detailed in [42]. In this step, the input file for ASCOT5 is created as well, using a method of transferring information from BEAMS3D to ASCOT5 which has been used in several previous works [36, 43].

Next, still using BEAMS3D, the markers representing ionized particles from the NBI are followed through the collisional slowing-down process, in which the trajectories of the charged particle gyrocenters are followed using the drift kinetic equations:

$$\frac{d\vec{R}}{dt} = \frac{\hat{b}}{qB} \times \left(\mu\nabla B + \frac{mv_{||}^2}{B}\left(\hat{b}\cdot\nabla\right)\vec{B} \right) + v_{||}\hat{b} + \frac{\vec{E}\times\vec{B}}{B^2} \quad (1)$$

$$\frac{dv_{||}}{dt} = -\frac{\mu}{m}\hat{b}\cdot(\nabla B) \quad (2)$$

where m is the particle's mass, q is its charge, $\vec{R}$ its position, $\hat{b} = \frac{\vec{B}}{B}$ is the direction of the magnetic field, $\mu = \frac{1}{2}\frac{mv_\perp^2}{B}$ is the magnetic moment, $v_{||} = \frac{d\vec{R}}{dt}\cdot\hat{b}(\vec{R})$ is the component of the velocity parallel to the magnetic field, and $\vec{E} = -\nabla\Phi$ is the electric field, which is assumed to only point perpendicular to $\hat{b}$ [44]. The effects of collisions and pitch angle scattering are included between integration time steps [43]. The markers representing fast ions are followed until they either thermalize or reach the last closed flux surface (LCFS) as defined in VMEC using the total enclosed toroidal flux given by NEOTRANSP, at which point they are considered lost. A preliminary validation and benchmarking of the code's slowing down model has already been performed [43].

From this simulation, the markers which reach the LCFS are saved and used to create many new markers (the exact number varies between the simulations and will be described in more detail in section 3). Each new marker is given a randomly assigned gyrophase and a random perturbation in pitch between −1 and 1%, while keeping the guiding center location and total energy the same. These newly created markers are used as the input for an ASCOT5 run, which follows them in full-orbit mode without collisions or electric field (due to the large uncertainties when specifying these quantities outside the LCFS) until these markers hit the wall, defined as a triangular mesh based on CAD models of W7-X's vacuum vessel and PFCs containing around 7.8 million mesh elements, with some simplification of the divertor and port geometries.

A detailed model of the NIFS-FILD head mounted on the MPM armature is included within this wall model. During the real experiment, some fraction of lost fast ions will pass through the pinhole and collimator of the detector and arrive on the sensor, contributing to the measured signal. However, it is simply not possible from a computational standpoint to track a sufficient number of markers to simulate this outright. For this reason, a method has been developed to find a simulated signal using a computationally tractable number of markers.

2.2. Simulating the NIFS-FILD

The difficulty in simulating signal to fast ion loss detectors lies in the impracticality of tracking a sufficiently large number of markers. The surface area of the LCFS for the W7-X equilibria used in this work is 134–141 m^2, and the surface area of the wall is even larger. Meanwhile, the area of the NIFS-FILD pinhole is 6.4×10^{-6} m^2. Even if the vessel wall had the same surface area as the LCFS, it would be necessary to simulate tens of millions of lost markers for a single one to reach the pinhole–and if that marker did not have the correct velocity vector at the pinhole, it might still have zero chance of making it through the pinhole and onto the sensor. To fully reproduce the signal, tens or hundreds of billions of simulated markers would need to be followed for tens or hundreds of milliseconds.

This work aims to develop an efficient simulation method though the use of two gyroorbit expansions, the first at the LCFS and the second at an intermediate virtual detection plane, to allow high fidelity simulation of fast ions arriving at the detector while using a computationally tractable number of simulation markers during the simulations from injection to the wall.

To achieve this goal, a virtual plane is created about 1 cm away from the pinhole along the direction of $\hat{b}$. Because the NIFS-FILD measures counter-going particles, which move along $-\hat{b}$, this means that any markers arriving at the pinhole will first pass through this plane. The plane is at constant toroidal angle ϕ, in order to make use of a built-in function of ASCOT5 for the simulations, and its extent in R and Z is determined by the area which can be reached by markers traced backwards in time from the pinhole, which spread out on the plane based on their initial velocity vector. In this way, the plane serves as a projection of the pinhole in velocity space. Figure 4 shows the virtual plane for the NIFS-FILD, along with the pinhole, sensor array, and example ion orbits.

The short distance between the plane and the pinhole means that the magnetic field does not change significantly between the two locations, keeping the gyroradius and pitch angle roughly constant, while still being large enough to project the pinhole onto a larger region of space: the area of the plane accessible from the pinhole is larger than the pinhole area itself by nearly a factor of 100, significantly lowering the number of markers that must be simulated.

As described in the previous subsection, lost markers are expanded to create a new, larger population of markers which are then followed to the wall. Using the 'Poincare' function in ASCOT5, the state of each marker (including position and velocity vectors, as well as the weight and time of flight) is saved each time it passes through the virtual plane, but it is not stopped; that is, the plane is treated as transparent.

These saved markers are divided into bins in 5D space, where the dimensions include the radial and vertical distances from the magnetic axis, R and Z, along with three velocity space coordinates:

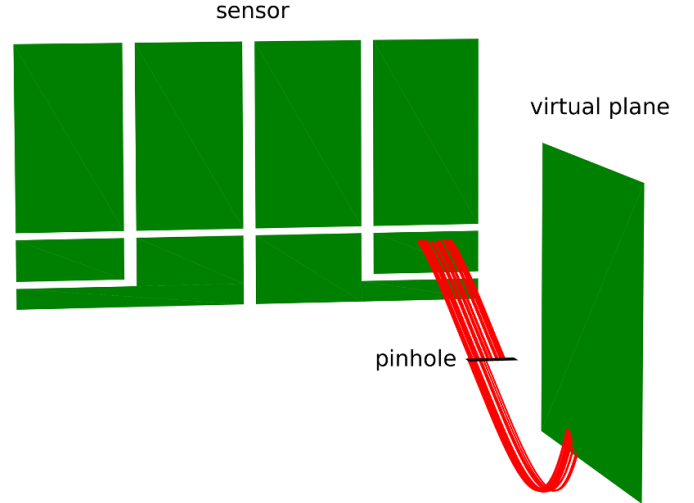$$\rho_L = \frac{mv}{|q|B} = \frac{v}{v_\perp} r_{\text{gyro}} \tag{3}$$

Figure 4. A 3D image showing the layout of the NIFS-FILD detector (left) and the virtual plane (right) with respect to the pinhole. Particle orbits, shown in red, travel forward in time from the pinhole to the detector, and backward in time from the pinhole to the plane. These orbits were simulated and the image was created using FILDSIM [45, 46].

$$\chi = \cos^{-1}\left(\frac{v_{||}}{v}\right) \tag{4}$$

$$\zeta = \tan^{-1}\left(\frac{-\hat{v}_\perp \cdot \left(\hat{b} \times \hat{z}\right)}{\hat{v}_\perp \cdot \hat{z}}\right) \tag{5}$$

where v is the magnitude of the total marker velocity $|\vec{v}|$, $v_\perp$ is the magnitude of the perpendicular velocity vector $|\vec{v}_\perp| = |\vec{v} - v_{||}\hat{b}|$, $\hat{v}_\perp$ is the direction of this vector $\frac{\vec{v}_\perp}{v_\perp}$, and $\hat{z}$ is the direction of the Z axis.

The quantity ρ_L, referred to as the 'gyroscalar' [47], is related to the marker gyroradius r_{gyro} by $\rho_L = \frac{v}{v_\perp} r_{\text{gyro}}$, and can be thought of as the path length traveled by the marker per radian of gyration. This convention is taken from the FILDSIM code [45, 46], which was not utilized for these simulations but inspired parts of the methodology. It will be given in units of cm. χ can be referred to as the pitch angle and will be given in degrees, while ζ is the gyrophase and will be given in radians to easily distinguish between the two angles.

By separating the markers into bins, we are in effect saying that each saved marker represents a cloud of markers, which could have any position-and-velocity-space coordinates within its bin. The initial analysis is performed with very small bins, which can then be combined to reach the bin size desired for the calculation of the signal. The initial size of the bins in (R, Z) space is shown in figure 5 and is close to 0.3 mm in each dimension. The initial size of the bins chosen for the other three coordinates are $\delta\chi = 0.25°$, $\delta\rho_L = 0.025$ cm, and $\delta\zeta' = \frac{2\pi}{900}$ (where ζ' is the gyrophase at the plane, as we are using ζ to describe the gyrophase at the pinhole).

For each 5D bin, we would like to know the probability that a marker randomly located within that bin will travel from the virtual plane to the pinhole of the NIFS-FILD, pass through the pinhole and collimating structure, and land on one
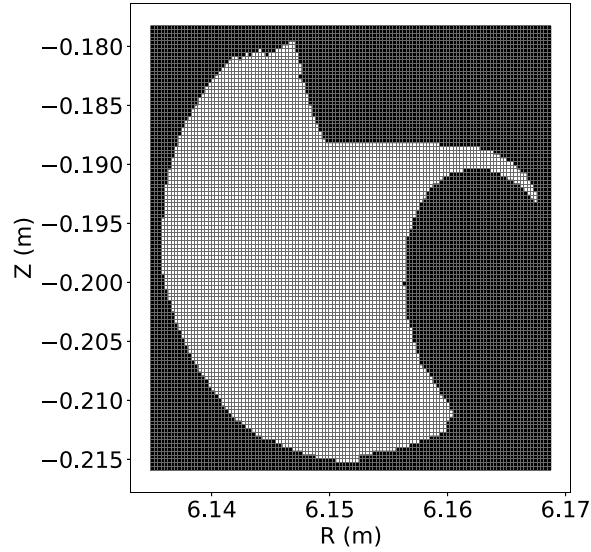
Figure 5. The plane of constant toroidal angle in front of the pinhole with a FILD insertion depth of 197 mm, divided into a grid in *R* and *Z*. The black rectangles represent those from which markers arriving from the LCFS have zero chance of passing through the pinhole.
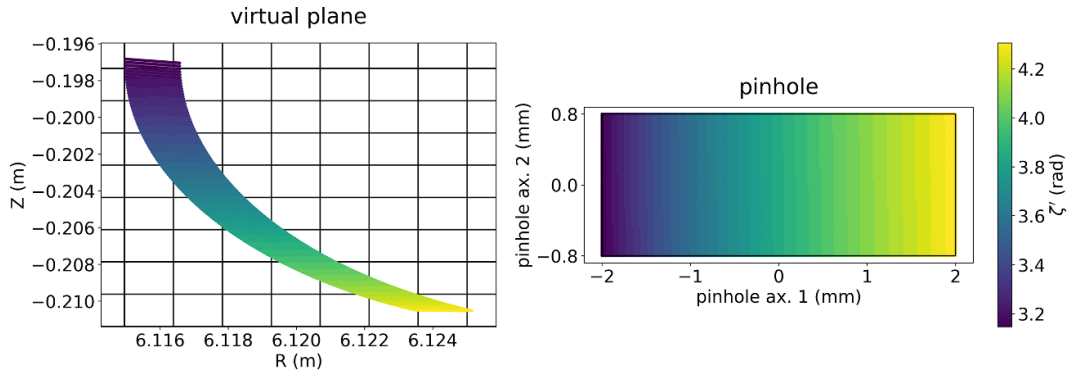

Figure 6. Markers with a single value of (χ, ρ_L, ζ) are traced backwards from the full area of the pinhole (right) to the virtual plane (left). These markers are color-coded in both the pinhole and on the plane by ζ', their gyrophase at the plane.

of the eight detectors. The following section will detail a geometric method for determining this probability, resulting in a 6D probability matrix (with the sixth dimension being the detector) that can be applied to any marker passing through the virtual plane in order to calculate its contribution to the signal.

2.3. A geometrical determination of probability

We begin by initializing markers within the pinhole, following them both forwards and backwards in time using ASCOT5 in full-orbit mode. The ones traced forwards are followed until they impact either the collimator or a sensor, while the ones traced backwards are followed until they impact the outside of the probe head or the virtual plane. Unlike in the simulations which follow markers from the LCFS, the plane is no longer transparent; when a marker impacts it, it is stopped.

To begin, we take a set of markers which have the same velocity vector in (χ, ρ_L, ζ) at the pinhole, with the magnetic field strength and direction at the center of the pinhole being used to calculate these quantities. The values chosen for this

demonstration of the method are (100°, 1.5 cm, 6.19 rad), and the markers are evenly distributed within the pinhole. We follow this set of markers forwards and backwards.

In figure 6(left), we can see the projection of the pinhole onto the virtual plane, while on the right side, we see the initial locations of the markers within the pinhole. (Note that for these examples, the grid applied to the virtual plane is larger than the one used in the actual analysis, for ease of illustration.) While the markers are initialized with the same gyrophase ζ, the gyrophase on the plane varies, and denoted as ζ'. The markers are color-coded by ζ'. In figure 7(top), we see the final location of the markers on the NIFS-FILD sensors, while on the bottom, we see the initial location within the pinhole of the markers which do (red) and do not (gray) make it to a sensor.

We can see several features in these figures that will simplify our analysis and reduce the number of necessary markers. In figure 7, we see that the initial locations of the markers which arrive at a sensor form one continuous region within the pinhole. Further tests of additional sets within phase space show that this is usually the case; occasionally, this region is
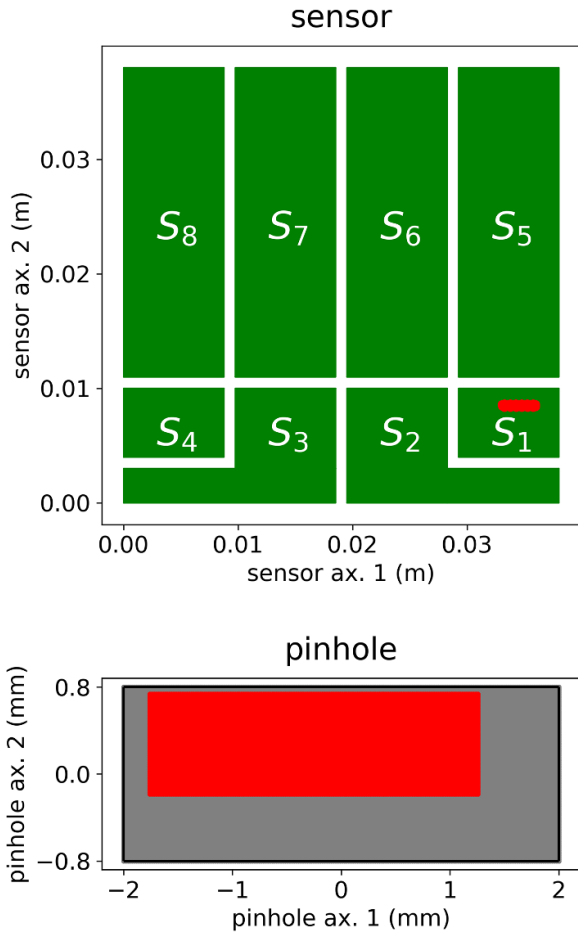
Figure 7. Markers with a single value of (χ, ρ_L, ζ) are traced forwards from the full area of the pinhole (bottom) to the detector (top), with markers that reach the detector denoted in red and those that do not in gray.

Figure 8. Markers with a single value of (χ, ρ_L, ζ) are launched forward from the pinhole in a cross-hatch pattern, with markers that reach the detector denoted in red and those that do not in black. The green box, defined by the extent of the red markers, is an estimate of the area within which markers launched can reach the detector.

a marker with (χ, ρ_L, ζ) launched anywhere within the pinhole reaching the sensor tile S_1 is thus the green shaded area in figure 8 divided by the total area of the pinhole:

$$P_{\chi, \rho_L, \zeta} \left(\text{pin} \to S_1 \right) = \frac{A_{\text{green}}}{A_{\text{pin}}}. \qquad (6)$$

For the backwards simulations, it is sufficient to launch markers along the long edges of the pinhole. These simplifications significantly reduce the number of required markers per set.

While the simulated markers are initialized with constant gyrophase at the pinhole, ζ, the goal is to determine the probability in terms of the gyrophase at the plane, ζ'. In order to do so, for a set of (χ, ρ_L, ζ), we choose a desired value of ζ': for this example, let it be $\zeta' = \frac{6}{5}\pi$ rad. We then look for the marker on each line (comprised of markers launched from the long edges of the pinhole and followed to the plane) which has ζ' closest to this value, and note the location of this marker both on the plane and at the pinhole, as shown in figure 9. The blue line represents the location within the pinhole along which markers launched backwards will reach the plane with our desired ζ', and the red line represents where these markers will strike the plane.

(A note on determining ζ': ASCOT5 simulations take longer to compute as the number of steps per gyroorbit is increased. For the backwards simulations, 180 to 360 steps per gyroorbit were used, but we desire to specify ζ' more precisely than this. As ζ' changes monotonically along the long edges of the pinhole, the actual value of ζ' is estimated by interpolation between neighboring markers.)

This process is repeated for a new set of markers. Let us define the original marker set as having (χ, ρ_L, ζ_1), then the second set has (χ, ρ_L, ζ_2), where $\zeta_1 = 6.19$ rad and $\zeta_2 = 6.236$ rad. In this way, we find the markers along the new set of strike lines with $\zeta' = \frac{6}{5}\pi$. This can be seen in figure 10, where the solid lines are the original set and the dashed lines are the new set.

The red lines denote the area within which a marker with $\zeta' = \frac{6}{5}\pi$ will arrive at the pinhole with a gyrophase $\zeta \in [\zeta_1, \zeta_2]$, and the blue lines denote the area of the pinhole at which these markers arrive. To find the probability of transmission from the plane to the pinhole for a marker in this group within one

divided into two sections, such as by the gap between adjacent sensors. In addition, the shape of this region is most often, but not always, a rectangle.

In figure 6, we see that the long edges of the pinhole define the outline of the pinhole on the plane; the markers launched from the short edges arrive much closer together and in straight lines. In addition, we see that contours of constant final gyrophase ζ' on the virtual plane (calculated using the magnetic field vector at the guiding center of each marker) form straight lines both on the plane and at the pinhole.

Further tests of additional sets within phase space show that this is always the case for the NIFS-FILD geometry, and that when part of the set of markers is prevented from reaching the plane by intersecting the exterior of the probe head, the dividing line between those that arrive at the virtual plane and those that do not is always a straight line both in the pinhole and on the plane.

This allows us to make several simplifications in our simulations. For the forward simulations, the markers can be launched in a cross-hatch pattern, as seen in figure 8, in order to determine the edges of the rectangular area. If this area is detected to be irregular, the simulation can be repeated with more markers in order to define its shape. The probability of
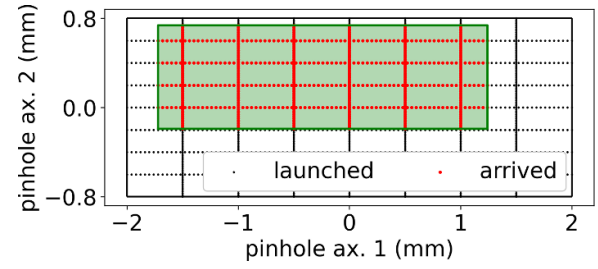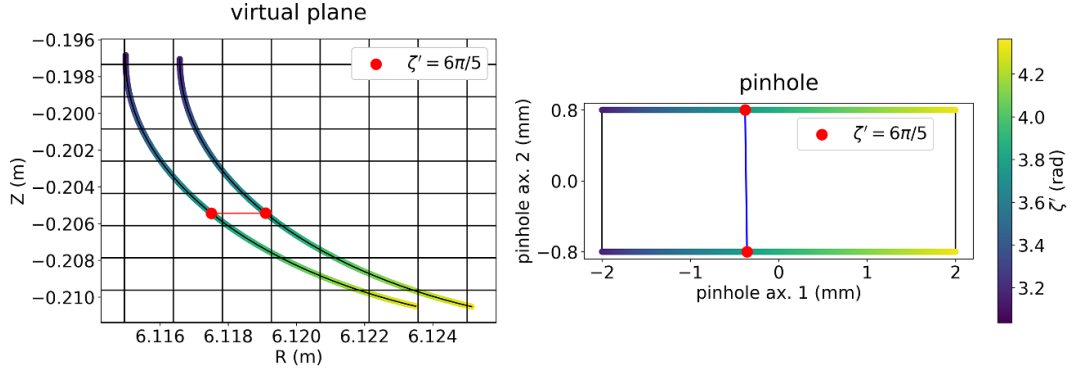
Figure 9. Markers with a single value of (χ, ρ_L, ζ) are launched backward from only the long edges of the pinhole (right) and followed to the virtual plane (left). The markers are color-coded both in the pinhole and at the plane by their gyrophase ζ' at the plane. The red dots denote the markers which have our desired value of ζ'.
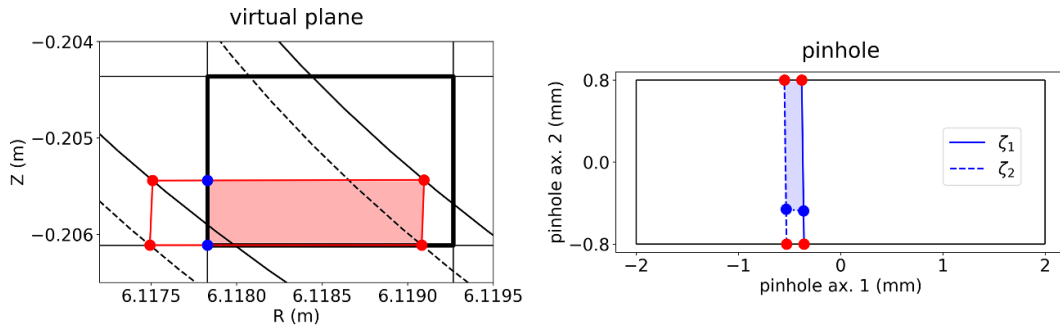

Figure 10. An outline at the plane (left) and in the pinhole (right) of those markers with our chosen (χ, ρ_L) which can travel between the two locations, have our chosen ζ' at the plane, and have $\zeta \in [\zeta_1, \zeta_2]$ at the pinhole. The bold black box at the plane represents a bin in (R, Z) space, and the blue dots represent the intersection of the red lines with this bold box. The shaded area represents where markers launched within this (R, Z) bin can pass through the pinhole within our gyrophase range.

(R, Z) bin outlined in bold on the left side of the figure, we find the area of the intersection between the red-outlined region and the bold-outlined box, and assume the intersections are located at the same percent of the distance along each line at the pinhole. The probability that a marker randomly located within this (R, Z) box, having a velocity (χ, ρ_L, ζ'), will arrive at the pinhole with $\zeta \in [\zeta_1, \zeta_2]$, is simply the red shaded area divided into the area of the bold-outlined (R, Z) box:

$$P_{R,Z,\chi,\rho_L,\zeta'} (\text{plane} \rightarrow \text{pin}|\zeta \in [\zeta_1, \zeta_2]) = \frac{A_{\text{red}}}{A_{RZ\,\text{box}}}. \quad (7)$$

It will see a reduced pinhole denoted by the blue shaded area.

In order to find the probability that these markers will then pass through the pinhole and onto the sensor, the backwards simulations are combined with the forward simulations. The forward simulation for the set with ζ_1 is now repeated for the set of markers with ζ_2, determining the outline of the green box, seen previously in figure 8, for this new set. Then, for each value of ζ at the pinhole, the intersection between the blue line (representing backwards transmission) and the green box (representing forwards transmission) is determined, as seen in figure 11.

The two lines of intersection combine to form a new quadrilateral, shaded purple in figure 11. Markers within the purple shaded region represent those which travel from the red shaded area in the (R, Z) plane, arrive to the pinhole with $\zeta \in [\zeta_1, \zeta_2]$,
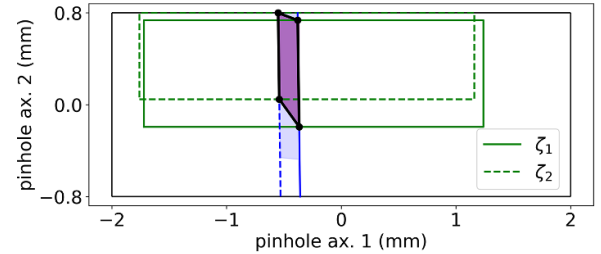
Figure 11. The probability of transmission through the pinhole is calculated by finding the area of intersection between the backwards and forwards simulations. For the two values of ζ at the pinhole, the intersection is taken between the line representing backwards transmission and the box representing forwards transmission, and these two lines of intersection are connected to form the shaded purple quadrilateral.

pass through the pinhole, and land on sensor S_1. The probability of transmission is this purple shaded area divided into the blue shaded area representing the pinhole as seen by these markers:

$$P_{\chi,\rho_L,\zeta'} (\text{pin} \rightarrow S_1|\zeta \in [\zeta_1, \zeta_2]) = \frac{A_{\text{purple}}}{A_{\text{blue}}}. \quad (8)$$

And thusly, the probability of a marker with our chosen (χ, ρ_L, ζ') coming from anywhere within the bold box in the
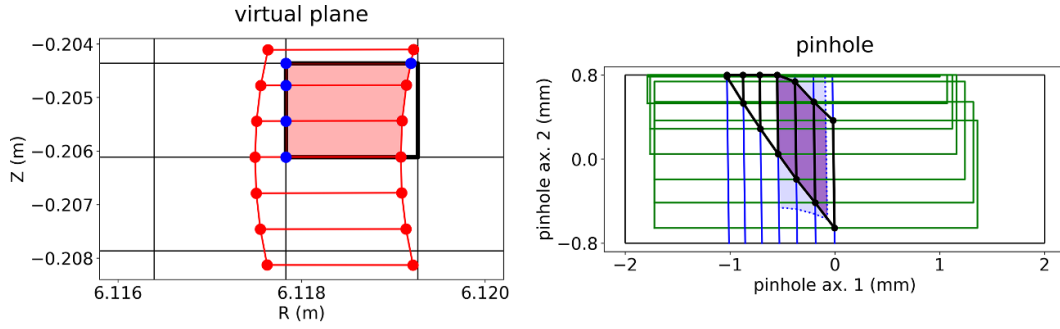
Figure 12. The total transmission probability is found by summing over all ζ bins at the pinhole the probability defined in equation (9). The areas used to calculate the probability, shown in this figure as the shaded regions, are restricted to those within our desired (R, Z) bin, shown as the bold black box on the virtual plane (left).

(R, Z) plane arriving to sensor S_1, while also having ζ within our specified bin at the pinhole, is

$$P_{R,Z,\chi,\rho_L,\zeta'}(\text{plane} \rightarrow S_1 | \zeta \in [\zeta_1, \zeta_2]) = \frac{A_{\text{red}}}{A_{RZ\,\text{box}}} \cdot \frac{A_{\text{purple}}}{A_{\text{blue}}}. \quad (9)$$

Finally, as the value of ζ at the pinhole is extraneous, we find the total probability by summing over the probability for every ζ bin at the pinhole,

$$\begin{aligned} P_{R,Z,\chi,\rho_L,\zeta'}(\text{plane} \rightarrow S_1) = &\sum_i P_{R,Z,\chi,\rho_L,\zeta'} \\ &\times (\text{plane} \rightarrow S_1 | \zeta \in [\zeta_i, \zeta_{i+1}]), \end{aligned}$$
$$(10)$$

with the resolution determined by the number of ζ values simulated. This can be seen in figure 12 for the specified (R, Z) box outlined in bold.

We would like to have bins in (χ, ρ_L, ζ'), rather than discrete values, and this is done by simply averaging the probability over several values of each quantity within a chosen bin. For the analysis in this work, 2 points in each of the three dimensions are averaged together to achieve bins of the smallest possible size, which can be further combined into larger bins. The result is a 6D probability matrix $P(S, R, Z, \chi, \rho_L, \zeta')$, where S denotes the channel of the sensor.

2.4. Combining the simulations

In order to form a signal, the probability matrix must be applied to the saved information of the markers arriving from the LCFS. Each marker, as it passes through the plane, is saved and sorted into a bin in $(R, Z, \chi, \rho_L, \zeta')$. Here, the marker's ρ_L is calculated based on B at the center of the pinhole, rather than at the plane, while the marker's pitch angle χ and gyrophase ζ' are calculated based on $\hat{b}$ at the marker's guiding center. The total velocity and pitch angle are assumed not to change between the pinhole and the plane—an assumption which is accurate for the total velocity, as the simulations are performed in the absence of collisions, but the pitch angle, as calculated in this work, can vary by up to about $0.22°$, on par with the smallest bin size. This was not found to make a difference to the simulated signal.

However, it was found that the number of markers passing through the plane was still not sufficient to calculate a simulated signal, and thus an additional step must be taken to improve marker statistics. For each marker at the plane, the gyrocenter is found and an expansion around it is performed, splitting the original marker into a ring of markers defined by the intersection of the virtual plane and a cylinder centered around the gyrocenter with an axis in the direction of $\hat{b}_{\text{gc}}$. The arrival time is kept the same for each new marker.

In order to make sure that each new marker in the ring could reach the virtual plane, the new markers are traced backwards for several gyroorbits. Some markers with large gyroradii are found to strike the exterior of the probe head and are thus removed from consideration; in future works, the need for this step could be avoided by positioning the virtual plane slightly further back from the pinhole. Once these markers are removed, the weight of the original marker is then evenly distributed among the remaining markers.

Finally, the probability matrix is applied to the new markers by multiplying the weight of each marker by $P(S, R, Z, \chi, \rho_L, \zeta')$, resulting in its contribution to the particle flux reaching each of the channels of the detector. This is combined with the arrival time of the marker and the duration of the NBI to produce a signal for each channel:

$$\begin{aligned} S_i(t) = &\sum_j w_j P\left(S_i, R_j, Z_j, \chi_j, \rho_{Lj}, \zeta_j'\right) \cdot (H(t - t_0) \\ &- H(t - (t_0 + T_{\text{NBI}}))) \end{aligned}$$
$$(11)$$

where j represents each marker, w_j is its weight, t_0 is the arrival time of each marker, T_{NBI} is the duration of the NBI, and H is the Heaviside step function, here used to create a box-car signal. As the NBI ions are protons, $S_i(t)$ is multiplied by 1.6×10^{-19} C to convert from particle flux to current. The total signal is then averaged over each sampling period of the NIFS-FILD digitizer, which is 2 μs.

During this step, the bin size can also be increased by averaging together neighboring probabilities and combining neighboring bins of arriving markers until the desired bin size is reached. It was found that the simulated signals converge for sufficiently small bins in (χ, ρ_L, ζ'), while for (R, Z), intermediate bin sizes must be used (between around 3×3 to 10×10
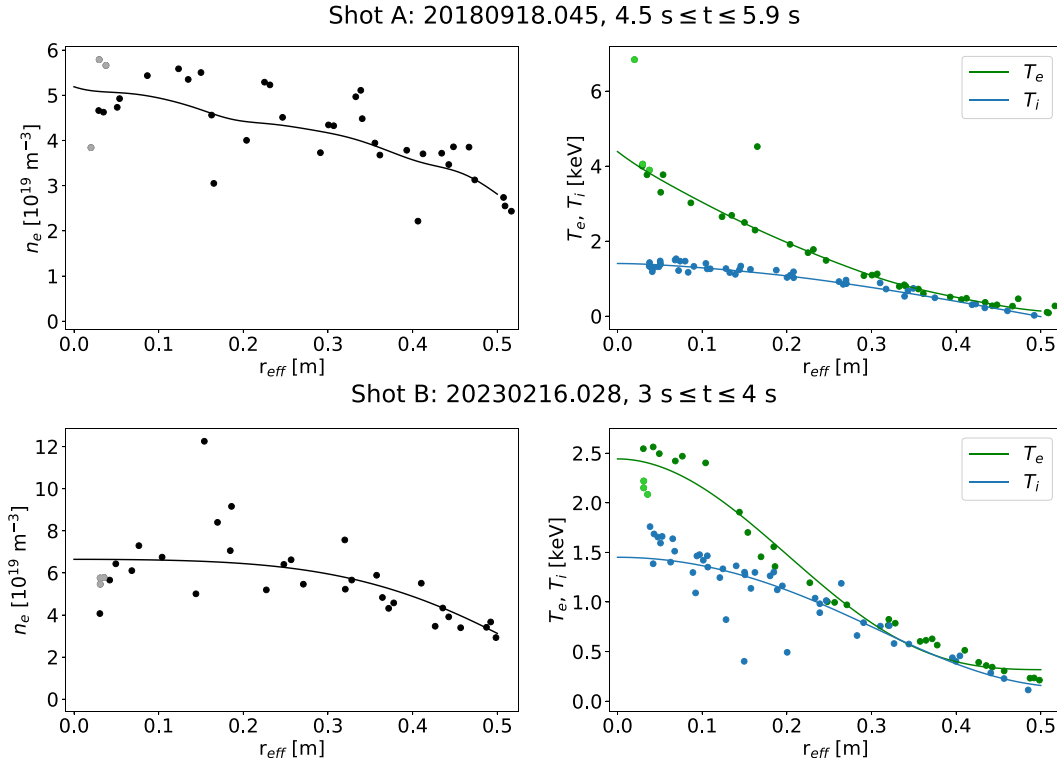
Figure 13. Experimentally measured density and temperature data for both shots simulated in this work, averaged over the given time intervals, with profiles fit. Points which were excluded from the fitting are plotted in a lighter color.

spatial bins; the exact best sizes vary between the simulations), as the signals diverge when the spatial bins are too large or small. As the largest change in the signal comes from the choice of (R, Z) bin size, signals were calculated for several intermediate bin sizes, and the difference was taken as a numerical uncertainty on the simulated signal, as will be shown in the following section.

3. Results and discussion

To validate this method, two real W7-X experiments were simulated, one from OP1.2b in 2018 and another from OP2.1 in 2023. The details of each experiment, which will be referred to in this work as Shot A and Shot B for simplicity, are as follows:

Shot A, from OP1.2b: 20180918.045, a hydrogen plasma in the W7-X standard magnetic configuration at 2.5 T. During this shot, NBI source 8 was fired in 10 ms blips separated by 100 ms intervals. Density and temperature profiles were averaged from 4.5 to 5.9 s into the shot, and the experimental signal to the NIFS-FILD was taken by averaging together the 4 NBI blips between 4.7 s and 5.1 s. During this time, the NIFS-FILD was inserted to a plunge depth of 197 mm, putting it at a major radius of $R = 6.141$ m. The NIFS-FILD data from this shot has been previously analyzed in [29] and simulated in [48] using a less detailed simulation method. As the neutralized power for these short beam blips is not certain, a nominal power of 1.8 MW was used for this simulation.

Shot B, from OP2.1: 20230216.028, a hydrogen plasma in the W7-X low-mirror configuration at 2.5 T. During this shot, NBI sources 4 and 7 were operated in steady-state for a duration of 5 s each, beginning at 2.0 and 2.1 s into the shot, respectively. This offset allows for the signal from each source to be separately identified. Density and temperature profiles were averaged from 3 to 4 s into the shot, by which point the density rise from the NBI had leveled off, and the signal to the NIFS-FILD is considered from 1.8 to 2.8 s, during which the NIFS-FILD was inserted to a plunge depth of 213 mm, putting it at a major radius of $R = 6.125$ m. After 2.8 s, the probe head was moved, but the profiles had stabilized to be nearly the same as those between 3 and 4 s, which is why the profiles from that time period were used–BEAMS3D simulations can only be performed using a single set of profiles, and it was desired to use steady-state profiles, rather than ones which were still evolving. The neutralized powers for the two neutral beam sources for this shot were determined by calorimetry to be 2.05 MW and 2.10 MW, respectively.

Experimentally measured temperature and density profiles for each shot, found by fitting data from Thomson scattering (n_e and T_e) and CXRS (T_i), are shown in figure 13. All profiles for Shot A were fit using a locally weighted scatterplot smoothing (LOWESS) method [49]. For Shot B, the n_e and T_i profiles were fit using a Gaussian process, while T_e was fit using a two-power function of the form $a(1 - s^b)^c$, where s is the flux surface coordinate and a, b, and c are the fitting parameters. These fitting methods were selected as they gave the smoothest profiles. For the Thomson data, n_e and T_e, three

Table 1. Percentage of injected energy lost to collisions with the port liner, shine-through, or through particle loss through the LCFS, or else absorbed into the plasma, for each simulation and beam source.

Simulation	Beam	Port	Shine.	Lost	Absorb.
Shot A	8	15.5%	17.4%	24.4%	42.7%
Shot B, n_e - 10%	4	15.3%	10.4%	27.7%	46.6%
Shot B, orig	4	15.3%	8.4%	28.4%	48.0%
Shot B, n_e + 10%	4	15.4%	6.7%	28.7%	49.3%
Shot B, n_e - 10%	7	7.9%	15.4%	41.1%	35.6%
Shot B, orig	7	7.9%	12.6%	42.7%	36.8%
Shot B, n_e + 10%	7	7.9%	10.5%	43.8%	37.7%
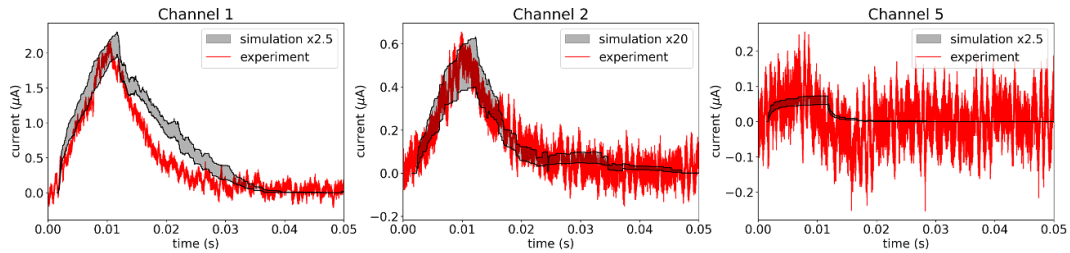
Figure 14. Experimental and simulated signals for three channels of the NIFS-FILD during Shot A. The simulated signals are scaled by the factors shown and shifted forwards in time by 1.5 ms.

channels were excluded from the fit, and those points are plotted in a lighter color.

Neutral beam deposition and slowing down for each shot were originally simulated in BEAMS3D with 2293 760 markers per beam component (with each source separated into components with full, one-half, and one-third energies) for Shot A, 655 360 markers per component for the initial run for Shot B, and 65 536 markers per component for density variation runs for Shot B, which were performed with density profiles both increased and decreased by 10%.

Table 1 shows the results of the deposition and slowing down simulations. The amount of energy lost due to collisions with the port liner is almost entirely determined by the beam source used, while the shine-through, as would be expected, decreases with increasing density. The ratio of lost to absorbed energy during the slowing down simulations does not vary significantly with density, but rather, both the total amount of lost and absorbed energy increase with density due to the decrease in shine-through.

For all four simulations (the initial simulations for each shot as well as the simulations for Shot B with varied density profiles), the markers at the LCFS were expanded into either 10 (for the initial simulations) or 100 (for the density scan) new markers for each lost marker, with random perturbations in pitch and randomly assigned gyrophase as described in section 2. The total number of markers run in this step was between 12 and 15.2 million for each simulation.

The experimental measurements and simulation results for three NIFS-FILD channels in Shot A are shown in figure 14. The five channels not shown have zero signal in the simulations and experimental signals equal to or lower than that of Channel 5, as seen in [48]. The experimental signal was conditioned by removing a DC component from before each NBI

blip, applying a noise filter, and averaging together the four blips from 4.7 to 5.1 s. The time axis shows the time since the beginning of the blip, when the NBI source first turns on. The simulated signals have been scaled and shifted 1.5 ms forward in time so that their time behavior can be compared to the experimental signals. The use of a band for the simulated signal represents the uncertainty introduced by the choice of bin size when calculating the signal.

The simulated signal underestimates the particle flux to Channels 1 and 5 by a factor of 2.5, similar to the simulations performed in [48] using a more simplistic method. The signal to Channel 2 is underestimated more significantly, by a factor of 20; later in this section, possible reasons for this discrepancy will be addressed. The rise time of the signal is well-matched for the two primary channels, while the fall time of Channel 1 is longer in simulation than reality.

Because the NBI blips only last 10 ms, the diagnostic information for the neutral beam source boxes is not acquired that quickly, and it may take longer than 10 ms for the beam parameters to stabilize, there is some uncertainty in the total power injected and the time which should be considered the true start time of NBI. As previously mentioned, there was not a reliable measurement of neutralized power for these beam blips, and so the simulations were performed simply using a nominal value for the input power.

We might expect the NBI-blip simulation to be less accurate than a simulation of steady-state NBI, during which there is plenty of time for the beam to both stabilize and be accurately measured. In addition, as the NBI system was still being commissioned during OP1.2b, the beam parameters used in the simulation may not be fully accurate. For all of these reasons, we would expect the simulations for Shot B, which was
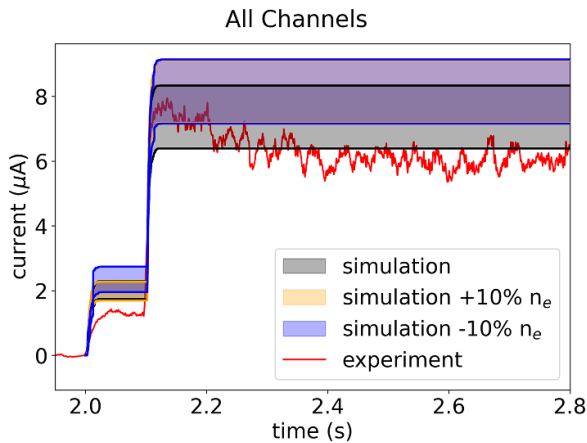
Figure 15. Simulated and experimental signals for Shot B summed over all NIFS-FILD channels, with the original density profile as well as the density scaled by $\pm 10\%$. Each signal is plotted as a band to represent the uncertainty introduced by the choice of bin size.

performed during OP2.1 with steady-state NBI, to be more accurate, and that is indeed what we see.

In figure 15, the total experimental signal during Shot B summed over all channels in the NIFS-FILD is compared to the total simulated signal with the density profile shown in figure 13(bottom), as well as with this density profile scaled by $\pm 10\%$, with the simulated signals again plotted as bands to represent the uncertainty in the choice of bin size. The experimental signal has had a DC component removed and a noise filter applied.

It can be seen that the simulated signal is very close to the experimental signal, and that the uncertainty introduced by varying the density is not larger than the uncertainty already present from the choice of bin size. After 2.1 s, the signals from the two density-scaled simulations overlap almost perfectly, although given the large uncertainty, this is not considered significant. The slight over-prediction is likely due to physical processes which are not accounted for in the simulation codes, particularly charge exchange within the scrape-off layer, which would be expected to decrease the signal if included in the model. The fact that changing the density does not alter the signal significantly is also unsurprising, since, as shown in table 1, the difference in total losses between the three simulations is only a few percent.

However, as we see in figure 16, the simulation does not properly predict the distribution of signal between the three channels which see the most significant particle flux. The signals to Channels 1 and 5 are over-predicted, while that to Channel 2 is under-predicted once again, as it was in Shot A. In addition, while it is not shown in the figure, there was some experimental signal to Channel 3, around 0.2 μA in steady-state, while the simulations showed no signal to this channel.

To analyze the beam sources separately, we take the signal from Source 4 for each channel as the signal at around 2.08 s,

and the signal from Source 7 to be the steady-state signal (averaged between 2.6 and 2.8 s) minus the signal from Source 4. In table 2 is shown the ratio between the simulated signal value, taken as the center of the band for the signal simulated using the original density profile, and the experimental signal for each beam. It can be seen that the simulated signal in Channel 1 is more accurate for Source 7 than Source 4, while the reverse is true for Channels 2 and 5. It can also be seen that the ratios between simulated and measured signal for Channels 1 and 5 are close for Source 4, but not Source 7; for Shot A, which used Source 8, these ratios were similar as well, and we might expect Sources 4 and 8 to be similar, as they inject at similar angles.

In order to determine the cause, a heat map showing the approximate particle flux onto these three sensors (in arbitrary units) for Source 4 and 7 during this shot is shown in figure 17. It can be seen that the flux from each beam is spread out in gyroscalar space, as plotted in figure 3, such that the strike pattern is centered on Sensor 1, with the very edges crossing over into Sensors 2 and 5.

If there were an error in the geometric model of the NIFS-FILD used in these simulations–for instance, if the sensors were tilted slightly with respect to the pinhole, or the entire probe head were rotated slightly on the MPM–the particle flux could be shifted upward in the plot, away from Sensor 2 and towards Sensors 1 and 5, compared to the experimental flux. A shift of even a millimeter or less could cause a significant change in the distribution of signals between the different sensors. However, this would not explain the lack of simulated signal to Channel 3, which is located far to the left of the particle flux, at higher pitch angle.

Another possible explanation could be an inadequacy of the physics included in the simulations. The simulated signal overestimates the measured flux of higher-energy fast ions and underestimates the flux of lower-energy ions. If this difference is present in all of the fast ions arriving at the probe head, rather than those that make it through the pinhole and onto the sensors (which would point to an error in the probe head or sensor positions, as described above), this could be due to several effects.

The simulations from the LCFS to the wall are performed collisionlessly. If the actual fast ions are slowing down significantly in the scrape-off layer, this would cause their arriving energies to be lower than those simulated, and thus shifted towards the bottom of the array of sensors. In addition, pitch angle scattering in the scrape-off layer could cause more fast ions with higher pitch angle to reach the FILD and be measured by Channel 3.

The ratios used for each of the three energy components of the beams (55 keV, 27.5 keV, and 18.3 keV) could be incorrect, overestimating the amount of full-energy particles injected as opposed to those in the half-or-third-energy components, again leading to a higher actual flux of lower-energy ions than predicted by simulation.

In addition, as the BEAMS3D slowing-down model has not yet been fully validated, the discrepancy could be caused by the fast ions losing more energy before they escape the plasma.
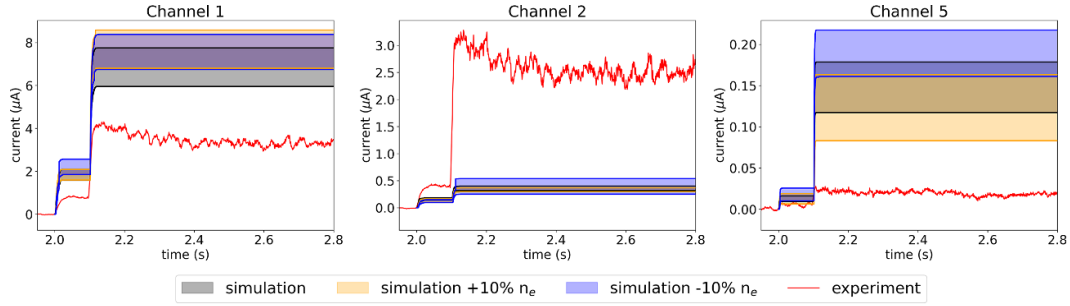
Figure 16. Simulated and experimental signals to the three individual detector channels with the highest signals for Shot B, with the original density profile as well as the density scaled by $\pm 10\%$. Each signal is plotted as a band to represent the uncertainty introduced by the choice of bin size.

Table 2. Factor by which the simulated signal under-or-over-predicts the experimental signal for Shot B.

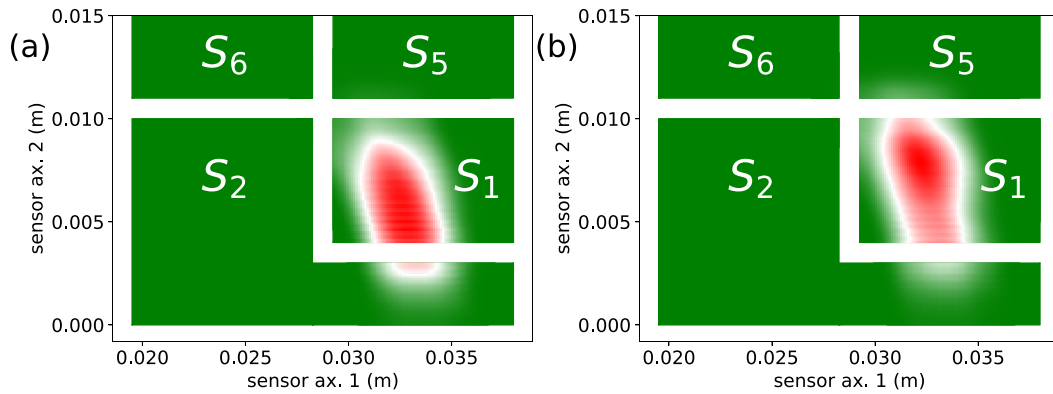| Beam	Channel 1	Channel 2	Channel 5
Source 4	2.4	0.39	2.0
Source 7	2.0	0.097	12.0
Combined	2.1	0.14	8.4

Figure 17. An approximate heat map of fast ion flux onto the NIFS-FILD sensors from NBI Sources 4 (*a*) and 7 (*b*).

The simulations were performed with a pure Z_{eff} of 1, both because BEAMS3D has not yet been validated with higher Z_{eff} and because of the difficulty in determining accurate Z_{eff} profiles throughout the plasma. A higher Z_{eff} might cause the fast ions to lose more energy to the plasma than predicted by these simulations.

In these simulations, the effect of charge exchange with neutrals, including both the halo around the beam and outside the LCFS, were not taken into consideration. In order to estimate the size of this effect, we used ADAS data [50] for charge exchange between protons and neutral hydrogen in the ground state to find the cross section for NBI-produced fast ions with energies of 55, 27.5, and 18.3 keV. The halo neutrals are a thermal population, so we assume they have an energy of 1.6 keV; the charge-exchange cross section σ_{CX} is then interpolated between ADAS data points to arrive at cross sections of 7.00×10^{-17}, 3.65×10^{-16}, and 5.25×10^{-16} cm^2 for the three energy levels of the NBI colliding with halo neutrals.

We assume, for the halo neutrals, an average density of 1×10^{15} m^{-3} and a full-width half-max of 0.125 m from the beam axis, both based on [51]. Taking the plasma circumference as $2\pi R_0 = 34.6$ m, where R_0, the major radius, is 5.5 m, and the two halo regions to be 0.25 m wide each, the fast ions are estimated to spend 1.4% of their time in the two beam halos. The frequency with which these fast ions experience a charge exchange process is thus $0.014 \cdot \sigma_{\text{CX}} \cdot n_{\text{halo}} \cdot v_{\text{ion}}$—for the three energy levels, this is calculated to be 0.334, 1.25, and 1.49 charge exchange processes per second. The ions from each of the three beam energy components which are lost in Shot B have an average time-of-flight between being ionized and crossing the LCFS of 5.0, 2.2, and 1.4 ms. Thus, we estimate that 0.17%, 0.28%, and 0.20% of the full, half, and one-third energy fast ions which are considered unconfined in our simulation would be lost to charge exchange with the halo neutrals, which is unlikely to affect our results.

For cold edge neutrals, the collision energy is assumed to be equal to the ion energies, and σ_{CX} is calculated at 7.26×10^{-17}, 3.93×10^{-16}, and 5.53×10^{-16} cm^2. An average neutral density of 3×10^{15} m^{-3} is assumed based on [52]. By the same process as above, considering only ground-state

hydrogen atoms as the edge neutrals, we calculate the number of charge exchange processes for each of the three energy levels as $\sigma_{CX} \cdot n_{neutral} \cdot v_{ion} = 70.7, 271,$ and 311 processes per second. The mean times-of-flight for fast ions which began at each of the three NBI energy levels between the LCFS and the virtual plane are 0.556, 1.11, and 1.74 ms. Thus, we estimate that 3.9%, 30%, and 54% of the fast ions at each of the three energy levels will be lost to charge exchange before reaching the virtual plane—though in actuality, this fraction would be even higher, as we have assumed that the fast ions did not slow down at all in the plasma.

Therefore, charge exchange with neutrals outside the LCFS is likely to reduce the signal measured by the FILD, though the exact impact would depend on the actual neutral density in the edge and the energy of the ions which leave the plasma. However, as it is the lower-energy ions which are preferentially lost, this cannot explain the fact that we measure more lower-energy fast ions with the NIFS-FILD than are predicted by simulation.

Another possible cause might be the energy-dependent redistribution of fast ions within the plasma due to instabilities. However, initial analysis of data from magnetic diagnostics on W7-X such as the Mirnov coils [53] and phase contrast imaging (PCI) [54] shows only weak mode activity which is unlikely to lead to significant changes to fast ion losses.

A final possibility would be a process such as alpha channeling, in which energy is channeled directly from the fast ions to the thermal ions, rather than to electrons [55]. This would lead to a higher ratio of lower to higher energy fast ions than predicted by simulation. However, the diagnostics of W7-X are not capable of performing an analysis at a fidelity high enough to determine whether this is the case.

A potential way to determine whether the discrepancy between simulated and measured signals to each channel is due to the fast ions arriving at the detector having lower energies than expected would be to look at predicted and measured heat fluxes to the NIFS-FILD head during operation, which would depend on the energy of the arriving fast ions as well as the total flux. Another option, to explore the possibility that the NIFS-FILD head position or position of the internal sensors differs from the model used in the simulations, would be to perform detailed metrology of the probe head in its installed and extended position on the manipulator arm.

4. Conclusion

A detailed model making use of gyroorbit expansion and a projection of the entrance aperture onto a virtual plane has been developed for simulating signals to the NIFS-FILD on W7-X. Simulations have been performed of experimental conditions from both NBI campaigns on W7-X, for both NBI blips and steady-state NBI, and quantitatively compared to measurement. Simulations of the NIFS-FILD signal from NBI blips agree with experiment within a factor of 3 for the channel with the highest signal and match the rise time of the signal well. Simulations of the signal from steady-state NBI show a very

close agreement between the total flux predicted and measured, though the distribution of this flux between the different channels of the detector does not match as closely.

The qualitative behavior of the discrepancy in the distribution of the signal between the FILD channels is the same for both simulated shots and all beam sources simulated, which is that the flux to the sensor array is shifted towards the sensors which measure the higher-energy fast ions. Possible explanations for this shift include either an error in the geometric model of the NIFS-FILD used in the simulations and/or its positioning on the MPM armature, or else an inadequacy of the physics included in the simulations, leading to arriving fast ions having lower energies than predicted. This could be the result of further slowing down in the scrape-off layer, an error in the assumed energy split of the neutral beams, an issue with the slowing-down model of BEAMS3D, differences between the actual and simulated Z_{eff} profile, instability-driven redistribution of fast ions within the plasma, or even a mechanism such as alpha-channeling.

Possible future areas of exploration include measuring the energy flux to the exterior of the NIFS-FILD and comparing this to simulation, or detailed metrology of the NIFS-FILD head for comparison to the CAD model.

This model has recently been expanded for use in simulating an additional FILD on W7-X, the S-FILD, and used to predict the total flux of fast ions to this diagnostic's scintillator plate as well as the spatial distribution of this flux [35]. A possible future step would be to apply this model to the FC-FILD as well.

ORCID iDs

A. LeViness https://orcid.org/0000-0002-2552-0411
S.A. Lazerson https://orcid.org/0000-0001-8002-0121

A. Jansen van Vuuren ⬤ https://orcid.org/0000-0003-1732-3642

J. Rueda-Rueda ⬤ https://orcid.org/0000-0002-4535-326X

M. Beurskens ⬤ https://orcid.org/0000-0002-3354-0279

S. Bozhenkov ⬤ https://orcid.org/0000-0003-4289-3532

K.J. Brunner ⬤ https://orcid.org/0000-0002-0974-0457

O.P. Ford ⬤ https://orcid.org/0000-0002-5646-4758

G. Fuchert ⬤ https://orcid.org/0000-0002-6640-2139

M. Garcìa-Muñoz ⬤ https://orcid.org/0000-0002-3241-502X

M. Isobe ⬤ https://orcid.org/0000-0002-3572-1882

C. Killer ⬤ https://orcid.org/0000-0001-7747-3066

J. Knauer ⬤ https://orcid.org/0000-0001-7359-6472

K. Ogawa ⬤ https://orcid.org/0000-0003-4555-1837

N. Pablant ⬤ https://orcid.org/0000-0001-6617-8459

P. Poloskei ⬤ https://orcid.org/0000-0001-7781-5599

T. Romba ⬤ https://orcid.org/0000-0002-2727-9385

References

[1] Gates D.A. *et al* 2018 Stellarator research opportunities: a report of the National Stellarator Coordinating Committee *J. Fusion Energy* **37** 51

[2] Bader A. *et al* 2020 Advancing the physics basis for quasi-helically symmetric stellarators *J. Plasma Phys.* **86** 905860506

[3] Beidler C.D. *et al* 2021 Demonstration of reduced neoclassical energy transport in Wendelstein 7-X *Nature* **596** 221–6

[4] Lazerson S.A. *et al* 2021 First neutral beam experiments on Wendelstein 7-X *Nucl. Fusion* **61** 096008

[5] Lazerson S.A. *et al* 2023 Neutral beam experiments with upgraded power on Wendelstein 7-X *29th IAEA Fusion Energy Conf. (FEC 2023)* (*London, UK, October 2023*)

[6] Warmer F., Beidler C.D., Dinklage A. and Wolf R. (the W7-X Team) 2016 From W7-X to a HELIAS fusion power plant: motivation and options for an intermediate-step burning-plasma stellarator *Plasma Phys. Control. Fusion* **58** 074006

[7] Andreeva T. *et al* 2004 The Helias reactor concept: comparative analysis of different field period configurations *Fusion Sci. Technol.* **46** 395–400

[8] Darrow D.S., Herrmann H.W., Johnson D.W., Marsala R.J., Palladino R.W. and Zwebens S.J. 1995 Measurement of loss of DT fusion products using scintillator detectors in TFTR (invited) *Rev. Sci. Instrum.* **66** 476

[9] Isobe M. *et al* 1999 Escaping fast ion diagnostics in compact helical system heliotron/torsatron *Rev. Sci. Instrum.* **70** 827

[10] Darrow D.S., Isobe M., Kondo T. and Sasao M. 1999 Enhancements to the Compact Helical System fast ion loss probe *Rev. Sci. Instrum.* **70** 838

[11] Darrow D.S., Werner A. and Weller A. 2001 Energetic ion loss diagnostic for the Wendelstein 7-AS stellarator *Rev. Sci. Instrum.* **72** 2936

[12] Werner A., Weller A. and Darrow D.S. (the W7-AS team) 2001 Fast ion losses in the W7-AS stellarator *Rev. Sci. Instrum.* **72** 780

[13] Garcia-Munoz M. *et al* 2007 NTM induced fast ion losses in ASDEX Upgrade *Nucl. Fusion* **47** L10

[14] Darrow D.S. 2008 Scintillator based energetic ion loss diagnostic for the National Spherical Torus Experiment *Rev. Sci. Instrum.* **79** 023502

[15] Garcia-Munoz M. *et al* 2008 Fast-ion losses due to high-frequency MHD perturbations in the ASDEX Upgrade tokamak *Phys. Rev. Lett.* **100** 055005

[16] Garcia-Munoz M., Fahrbach H.U. and Zohm H. (the ASDEX Upgrade Team) 2009 Scintillator based detector for fast-ion losses induced by magnetohydrodynamic instabilities in the ASDEX Upgrade tokamak *Rev. Sci. Instrum.* **80** 053503

[17] Garcia-Munoz M. *et al* 2009 MHD induced fast-ion losses on ASDEX Upgrade *Nucl. Fusion* **49** 085014

[18] Fisher R.K. *et al* 2010 Scintillator-based diagnostic for fast ion loss measurements on DIII-D *Rev. Sci. Instrum.* **81** 10D307

[19] Garcia-Munoz M. *et al* 2010 Convective and diffusive energetic particle losses induced by shear alfvén waves in the ASDEX Upgrade tokamak *Phys. Rev. Lett.* **104** 185002

[20] Ogawa K. *et al* 2010 Observation of energetic-ion losses induced by various MHD instabilities in the Large Helical Device (LHD) *Nucl. Fusion* **50** 084005

[21] Chen X., Fisher R.K., Pace D.C., García-Muñoz M., Chavez J.A., Heidbrink W.W. and Van Zeeland M.A. 2012 Near midplane scintillator-based fast ion loss detector on DIII-D *Rev. Sci. Instrum.* **83** 10D707

[22] Kim J., Kim J.Y., Yoon S.W., García-Muñoz M., Isobe M. and Kim W.C. 2012 Initial measurements of fast ion loss in KSTAR *Rev. Sci. Instrum.* **83** 10D305

[23] Garcia-Munoz M. *et al* 2013 Fast-ion losses induced by ELMs and externally applied magnetic perturbations in the ASDEX Upgrade tokamak *Nucl. Fusion* **55** 124014

[24] Chang J.F., Isobe M., Ogawa K., Huang J., Wu C.R., Xu Z., Jin Z., Lin S.Y. and Hu L.Q. 2016 Scintillator-based fast ion loss measurements in the EAST *Rev. Sci. Instrum.* **87** 11E728

[25] Garcia-Munoz M. *et al* 2016 Conceptual design of the ITER fast-ion loss detector *Rev. Sci. Instrum.* **87** 11D829

[26] Yamamoto S. *et al* 2016 Faraday-cup-type lost fast ion detector on Heliotron J *Rev. Sci. Instrum.* **87** 11D818

[27] Jin Z. *et al* 2017 Extended scintillator-based fast-ion loss diagnostic in the EAST *Fusion Eng. Des.* **125** 160

[28] Sanchis L. *et al* 2019 Characterisation of the fast-ion edge resonant transport layer induced by 3D perturbative fields in the ASDEX Upgrade tokamak through full orbit simulations *Plasma Phys. Control. Fusion* **61** 014038

[29] Ogawa K. *et al* 2019 Energy-and-pitch-angle-resolved escaping beam ion measurements by Faraday-cup-based fast-ion loss detector in Wendelstein 7-X *J. Inst.* **14** C09021

[30] Lazerson S.A., Ellis R., Freeman C., Ilagan J., Wang T., Shao L., Allen N., Gates D. and Neilson H. 2019 Development of a Faraday cup fast ion loss detector for keV beam ions *Rev. Sci. Instrum.* **90** 093504

[31] Kulla D., Lazerson S.A., Hunger K., Gerdes H. and Bandorf R. 2023 Layer thickness characterization of Faraday cup fast ion loss detectors *Rev. Sci. Instrum.* **94** 053503

[32] Nicolai D. *et al* 2017 A multi-purpose manipulator system for W7-X as user facility for plasma edge investigation *Fusion Eng. Des.* **123** 960

[33] van Vuuren A.J. *et al* 2022 Conceptual design of a scintillator-based fast-ion loss detector for the Wendelstein 7-X Stellarator *IEEE Trans. Plasma Sci.* **50** 4114

[34] van Vuuren A.J. *et al* 2024 Development of a scintillator based fast-ion loss detector for the Wendelstein 7-X stellarator *Fusion Eng. Des.* **204** 114520

[35] LeViness A. *et al* 2024 Simulation of a scintillator-based fast ion loss detector for steady-state operation in Wendelstein 7-X *Rev. Sci. Instrum.* **95** 073529

[36] Kulla D., Lazerson S.A., Günter S., Hirsch M., Hartmann D., McNeely P., Rust N. and Wolf R.C. 2022 Placement of a fast ion loss detector array for neutral beam injected

particles in Wendelstein 7-X *Plasma Phys. Control. Fusion* **64** 035006

[37] Bozhenkov S.A. *et al* 2017 The Thomson scattering diagnostic at Wendelstein 7-X and its performance in the first operation phase *JINST* **12** 10004

[38] Ford O.P. *et al* 2020 Charge exchange recombination spectroscopy at Wendelstein 7-X *Rev. Sci. Instrum.* **91** 023507

[39] Hirschman S.P. and Whitson J.C. 1983 Steepest-descent moment method for three-dimensional magnetohydrodynamic equilibria *Phys. Fluids* **26** 3553

[40] Haken S. 2021 Neotransp (available at: https://gitlab.mpcdf. mpg.de/smithh/neotransp)

[41] Hopf C. 2017 Scaling of the neutral beam shine through power for each source as a function of beam isotope, density, and beam acceleration voltage (available at: www.aug.ipp.mpg. de/foswiki/pub/ITED/NiauOpDiagrams/ShineThrough Scaling.pdf)

[42] Lazerson S.A. *et al* 2020 Validation of the BEAMS3D neutral beam deposition model on Wendelstein 7-X *Nucl. Fusion* **60** 076020

[43] Lazerson S.A. *et al* 2021 Modeling and measurement of energetic particle slowing down in Wendelstein 7-X *Nucl. Fusion* **61** 096005

[44] McMillan M. and Lazerson S.A. 2014 BEAMS3D neutral beam injection model *Plasma Phys. Control. Fusion* **56** 095019

[45] Rueda-Rueda J. *et al* 2024 FILDSIM (https://doi.org/ 10.5281/zenodo.12512086)

[46] Rueda-Rueda J. *et al* 2024 Tomographic reconstructions of the fast-ion phase space using imaging neutral particle analyser measurements *Plasma Phys. Control. Fusion* **66** 065025

[47] Schmidt B.S. *et al* 2024 Anisotropic regularization for inversion of fast-ion loss detector measurements (submitted)

[48] Äkäslompolo S. *et al* 2019 Validating the ASCOT modelling of NBI fast ions in Wendelstein 7-X stellarator *J. Inst.* **14** C10012

[49] Cleveland W.S. *et al* 1979 Robust locally weighted regression and smoothing scatterplots *J. Am. Stat. Assoc.* **74** 829–36

[50] Summers H.P. 2004 Adas the ADAS User Manual (version 2.6) (available at: www.adas.ac.uk)

[51] Bannmann S. *et al* 2023 Fast forward modeling of neutral beam injection and halo formation including full Balmer-α emission prediction at W7-X *J. Instrum.* **18** 10029

[52] Winters V.R. *et al* 2021 EMC3-EIRENE simulation of first wall recycling fluxes in W7-X with relation to H-alpha measurements *Plasma Phys. Control. Fusion* **63** 045016

[53] Rahbarnia K. *et al* 2021 Alfvénic fluctuations measured by in-vessel Mirnov coils at the Wendelstein 7-X stellarator *Plasma Phys. Control. Fusion* **63** 015005

[54] Huang Z. *et al* 2021 The Wendelstein 7-X phase contrast imaging diagnostic *J. Instrum.* **16** 01014

[55] Fisch N.J. 2015 The alpha channeling effect *AIP Conf. Proc.* **1689** 020001